ICCFD13 MILAN ITALY 2026

ICCFD13-2026-179

Effects of Chordwise-Slit Parameter Variations on the Lift Performance of an Aircraft Flap

E. Kobayashi* and K. Chiba*
Corresponding author: k2442006@edu.cc.uec.ac.jp
* The University of Electro-Communications, Japan

Abstract: This study examines the aerodynamic effects of introducing multiple chordwise slits into a single-slotted aircraft flap. At high deflection angles during takeoff and landing, boundary-layer separation develops on the upper surface of the flap, with its extent varying along the span due to three-dimensional flow. To mitigate this problem, chordwise slits were incorporated to divide the flap into segments, aiming to suppress separation and allow spanwise variation in flap geometry. As an initial step toward spanwise-varying flap designs, our study investigates the aerodynamic consequences of introducing slits and varying their geometric parameters. Numerical simulations were performed for flaps with different slit lengths, numbers, and widths, and their lift characteristics were compared with the conventional flap. The results show that an optimal slit configuration can increase the lift coefficient by up to 4.7% compared to a conventional flap without slits. However, this benefit comes with a tradeoff: the slits accelerate pressure recovery upstream, raising the pressure near the flap's leading edge.

Keywords: Aircraft flap, Computational fluid dynamics, Aerodynamic performance, Flow separation control.

1. Introduction

High-lift systems are movable aerodynamic components mounted on aircraft wings. The aerodynamic design of modern transport aircraft is generally optimized for cruise flight [1]; however, lift becomes insufficient during the low-speed phases of takeoff and landing. To compensate, high-lift devices are deployed to augment lift during these conditions. According to Boeing [2], a 1% improvement in the lift-to-drag ratio L/D during takeoff can increase payload capacity by roughly 2,800 lb, while a 1.5% rise in maximum landing lift can yield up to 6,600 lb of additional payload. Hence, developing high-lift systems that more effectively improve takeoff and landing performance offers substantial potential for reducing fuel consumption, environmental impact, and operational cost.

High-lift devices are broadly categorized as leading-edge or trailing-edge flaps. During cruise, these elements remain retracted along the wing edges, and they are extended forward or rearward during takeoff and landing. Leading-edge flaps help delay flow separation on the upper surface by channeling airflow from the lower side through the slot, thereby energizing the boundary layer and postponing stall [3]. Trailing-edge flaps, in contrast, enlarge the wing area and camber, reducing static pressure near the trailing edge. They also allow air from beneath the wing to flow over the flap's upper surface, suppressing separation and further enhancing lift [3]. However, as the deflection angle increases, boundary-layer separation tends to develop on the flap's upper surface, diminishing lift [4, 5].

To mitigate such separation, multi-slotted flaps with two or three slots have been widely adopted. These additional gaps promote more uniform airflow over the flap surface, effectively delaying separation [6, 7]. The major drawback, however, is the accompanying increase in structural weight. As another passive technique, vortex generators have been used to energize the boundary layer and postpone stall [8, 9]; yet, the induced vortices inevitably increase drag C_D [5]. Active flow-control concepts—such as dielectric-barrier-discharge plasma actuators [10, 11] and steady or pulsed jet blowing [12]—have also been investigated. While effective, these approaches require electrical power, and achieving adequate control

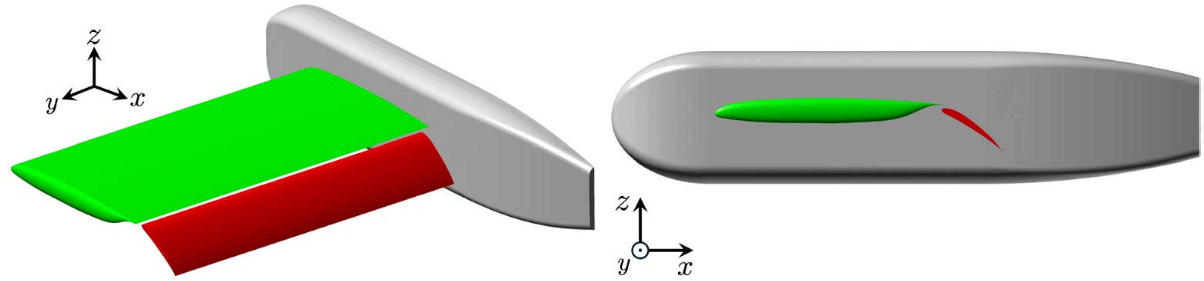

Figure 1: Configuration of the computational model, consisting of a wing (green), a single-slotted flap (red), and a fuselage (gray). (a) Bird's-eye view of the model; (b) Side view.

over the large surface of a commercial wing demands significant onboard energy resources [13].

In conventional slotted-flap mechanisms operating on fixed tracks [14], the spanwise gap between the main wing and flap is constant and cannot adapt to three-dimensional flow variations. Morphing-flap concepts have been explored to overcome this limitation [15, 16, 17], but without discrete spanwise gaps, they cannot fully accommodate local flow variations. To address this issue, Chiba et al. [18, 19] proposed a yaw-rotatable flap that introduces a spanwise-varying gap, achieving up to a 3.3% lift increase. However, the variation in that design was linear along the span and could not fully optimize the flap geometry for local separation characteristics.

Building on this idea, the present study proposes segmenting the flap spanwise so that each section can adapt to local aerodynamic conditions. As an initial step toward a spanwise-adaptive configuration, we investigate the aerodynamic effects of introducing chordwise slits—narrow gaps dividing the flap into segments—on lift performance. Sigrest et al. [20, 21] showed that multiple slits near a wing's trailing edge can drive airflow from the lower to the upper surface, re-energizing the boundary layer and delaying stall. Inspired by their findings, we hypothesize that similar slits on a single-slotted flap can suppress separation on the upper surface and thereby enhance lift. Demonstrating this would enable control of boundary-layer separation on conventional flaps without the need for additional devices or active control systems. Furthermore, this study focuses primarily on clarifying the extent of the aerodynamic benefits induced by the slits, while the impacts on noise and structural feasibility are left for future investigation. The influence of slit geometry is also expected to be significant; therefore, this work conducts a parametric analysis of slit length, number, and width, together with an examination of the underlying flow mechanisms.

The remainder of this paper is organized as follows. Section 2 describes the computational framework, including model geometry, mesh generation, and numerical methods. Section 3 compares the aerodynamic performance of the optimal slit configuration with that of the baseline flap and discusses the mechanisms responsible for the observed lift enhancement. Section 4 explores the effects of individual slit parameters, and Section 5 summarizes the conclusions and outlines directions for future research.

2. Computational setup

2.1 Configurations

Since the primary objective of this study is to investigate the aerodynamic effects of introducing slits into the flap, a simplified configuration consisting of a fuselage, a main wing, and a single slotted flap, as shown in Fig. 1, is employed. The geometry was created using OpenVSP [22], with minor modifications made in Autodesk Fusion 360. Details of each component are given below.

Main wing: The wing design is based on "OTOMO" [23], which was developed by Japan Aerospace Exploration Agency (JAXA) for aerodynamic noise reduction research. For simplification, the wing

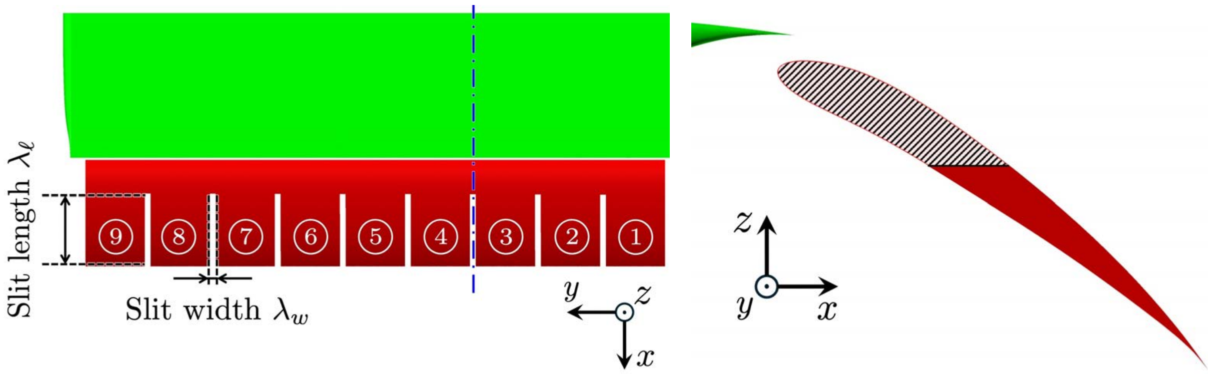

Figure 2: Flap geometry with eight chordwise slits. (a) Top view of the slitted flap, showing the segment divisions along the span. (b) Cross-sectional profile of the flap taken at the location indicated by the blue dashed line in (a), illustrating the slit shape and orientation.

Table 1: Parameters for the parametric studies of slit geometry. For each parameter (λ_ℓ, N, λ_w), the left column lists the values tested, while the right column shows the other two parameters held constant (fixed at the preliminary optimal: $\lambda_\ell = 50\% c_{\text{flap}}$, $N = 8$, $\lambda_w = 1.0\% b_{\text{flap}}$). (Note: λ_ℓ is given as a percentage of flap chord, and λ_w as a percentage of flap span.)

	Values in the left column	Values of the other two parameters
Length λ_ℓ (Ratio to c_{flap})	40%, 50%, 60%, 100%	$N = 8$, $\lambda_w = 1.0\% b_{\text{flap}}$
Number N	4, 8, 12	$\lambda_\ell = 50\% c_{\text{flap}}$, $\lambda_w = 1.0\% b_{\text{flap}}$
Width λ_w (Ratio to b_{flap})	0.25%, 0.5%, 1.0%, 2.0%	$\lambda_\ell = 50\% c_{\text{flap}}$, $N = 8$

planform is modeled as a rectangular shape, and the wing's cross-sectional profile adopts the JAXA Standard Model airfoil. In addition, the wingtip is rounded to suppress wingtip vortices.

Flap: The flap geometry used in this study is derived from the configuration employed in the OTOMO model. The flap's chord c_{flap} and span b_{flap} are 30% and 95% of those of the main wing, respectively. The flap's planform is truncated vertically at the root and tip. In the simulations, the flap deflection angle is 35.0°. The gap and overlap between the main wing and flap are $0.01628 c_{\text{main}}$ and $0.01 c_{\text{main}}$, respectively (with c_{main} the main wing chord). These values correspond to the OTOMO landing configuration.

The geometry of the slitted flap is shown in Fig. 2. As shown in Fig. 2, each wing element separated by the slits is assigned an index and referred to as the 1st, 2nd segment, and so on, from the wing root outward. As illustrated in Fig. 2, the slits are cut such that each cut plane is aligned parallel to the x-y plane. This orientation is intended to reduce flow separation caused by slit corners and to promote smoother airflow through the slits.

In this study, we conducted a parametric investigation of slit length λ_ℓ, number of slits N, and slit width λ_w, using the combinations shown in Table 1. The definitions of λ_ℓ and λ_w are shown in Fig. 2. When performing a parametric study for one of these parameters, the other two parameters are fixed at the values that yielded the highest C_L.

Fuselage: For the fuselage, we use the geometry from NASA's trapezoidal-wing high-lift model (from the First AIAA CFD High-Lift Prediction Workshop [24]).

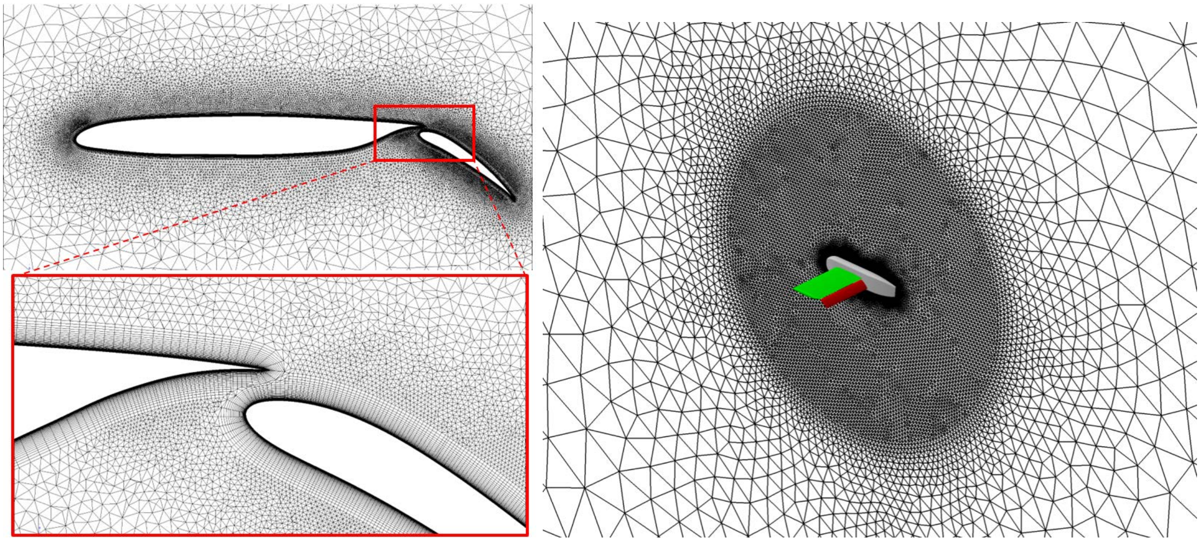

Figure 3: Cross-sectional views of the volume mesh. (a) Mesh cut at mid-span (50% span), including a close-up of the flap's leading-edge region. (b) Mesh cut on the symmetry plane (fuselage centerline).

2.2 Mesh generation

Unstructured meshes were generated using MEGG3D [25, 26], which enables automated mesh generation with high flexibility. As shown in Fig. 2.2, prismatic layers were applied near the surface to resolve the boundary layer flow. The first-layer thickness, stretching factor, and the maximum number of prism layers were set to $0.01/\sqrt{Re}$, 1.12, and 50, respectively. Re signifies Reynolds number. The computational domain was defined as a hemisphere with a radius 15 times the fuselage length.

In the present numerical analysis, the narrow slit gaps were expected to induce highly complex flow structures. Consequently, as illustrated in Fig. 2.2, a two-tier mesh refinement strategy was adopted. First, the mesh was locally refined within a hemispherical region of radius 2 fuselage lengths around the model to capture detailed flow features. Additional local refinement was applied near the slits to resolve the complex flow in these gaps. Further increasing the mesh density did not change C_L by more than 0.3%, indicating mesh independence.

The mesh for the non-slit model comprised approximately 0.59 million surface nodes and 34.9 million volume nodes. The flap models with slits contained approximately 0.58 million surface nodes and 35.0 million volume nodes.

2.3 Flow solver

We used JAXA's compressible flow solver FaSTAR [27] (ver. 6.0.7) for all simulations. This solver employs an unstructured, node-centered finite volume method with MUSCL-type reconstruction [28] and Hishida's differentiable slope limiter [29] to achieve second-order spatial accuracy for the 3D RANS equations. For the numerical flux, we applied the HLLEW scheme [30], and for time integration we used the LU-SGS scheme [31]. Turbulence was modeled with an Explicit Algebraic Reynolds Stress Model (EARSM) [32, 33] based on a k-ω formulation.

Figure 4 presents the convergence history of C_L for the slit model yielding the maximum C_L ($\lambda_\ell = 50\% c_{\text{flap}}$, $N = 8$, $\lambda_w = 1.0\% b_{\text{flap}}$), compared with the non-slit case. For the slit model, changes fall below 1×10^{-4} in magnitude, indicating convergence after 50 000 steps. By contrast, the non-slit model exhibits oscillatory behavior caused by unsteady fluctuations in the large separation region on the flap's upper surface, which affect the pressure distributions on both the flap and the main wing. Convergence for this case is taken at 150 000 steps, where the oscillation mean becomes nearly constant and the

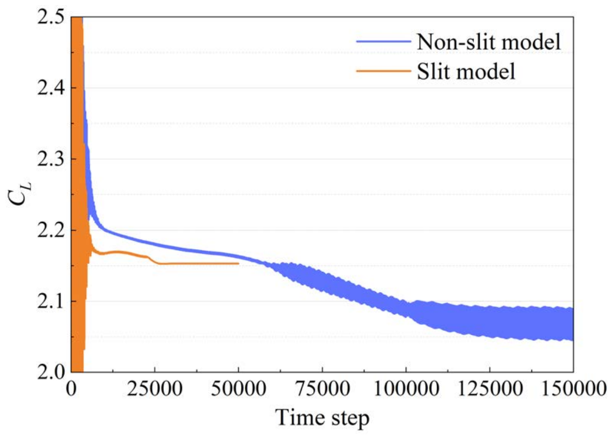

Figure 4: Convergence histories of C_L for the non-slit model and the slit model ($\lambda_\ell = 50\%c_{\text{flap}}$, $N = 8$, and $\lambda_w = 1.0\%b_{\text{flap}}$). For the slit model, convergence is achieved within 50 000 steps. The non-slit model shows oscillatory behavior, but after approximately 150 000 steps the mean C_L value stabilizes, and the peak-to-peak oscillation amplitude stays around 2%.

peak-to-peak variation reduces to about 2%. For other slit models that show oscillations, we assess convergence in the same manner as for the non-slit case. In the results that follow, the final iteration is reported for models converging within 1 count, while for oscillatory cases, the time-averaged solution over the last 10 000 steps is used.

All computations were performed on a local cluster of five nodes, each with an Intel Xeon E5-2660 (2.2 GHz, 16 cores) and 64 GB of RAM. The computational time was approximately 180 hours for the non-slit model, 75 hours for the slit model ($\lambda_\ell = 50\%c_{\text{flap}}$, $N = 8$, $\lambda_w = 1.0\%b_{\text{flap}}$). The non-slit model required approximately 2.5 times more iterations to reach convergence than the slit configurations, owing to unsteady fluctuations in the large separation region on the flap upper surface as noted above.

2.4 Computational conditions

Assuming the landing conditions of OTOMO, the angle of attack α is set to 8.0° and the freestream Mach number M to 0.20. The Reynolds number Re (based on the wing chord) is defined as $Re = 4.3 \times 10^6$.

3. Results: baseline vs. slit case

The parametric study showed that the slit model with $\lambda_\ell = 50\%c_{\text{flap}}$, $N = 8$, $\lambda_w = 1.0\%b_{\text{flap}}$ achieved the highest C_L, exceeding that of the non-slit model. Therefore, in this section, we compare the flow field of the highest-C_L slit configuration to that of the non-slit model to elucidate the mechanism behind the lift enhancement. Figure 5 presents the aerodynamic coefficients for the two models.

As shown in Fig. 3, the slit configuration exhibits an overall C_L improvement of 4.7% compared to the non-slit model, with increases of 4.1% for the main wing and 7.4% for the flap. Meanwhile, the overall C_D of the slit model is 8.0% higher than that of the non-slit model, with increases of 6.8% for the main wing and 6.6% for the flap. This rise is attributed to additional induced drag caused by the higher C_L of each component and by vortices generated at the slit corners. As a result, the L/D decreased by 3.0% compared to the non-slit model. It is assumed that adding slits (i.e., dividing the flap into segments) can be achieved with manageable structural and mechanical complexity — a premise that future work should verify.

Because the simulation represents a landing condition, we focus on lift (C_L). To investigate the factors contributing to this C_L enhancement, Fig. 6 presents the surface pressure coefficient C_p, surface streamlines, and separation regions (the isosurfaces of streamwise velocity $u_{\text{vel}} = 0$). These visualizations reveal

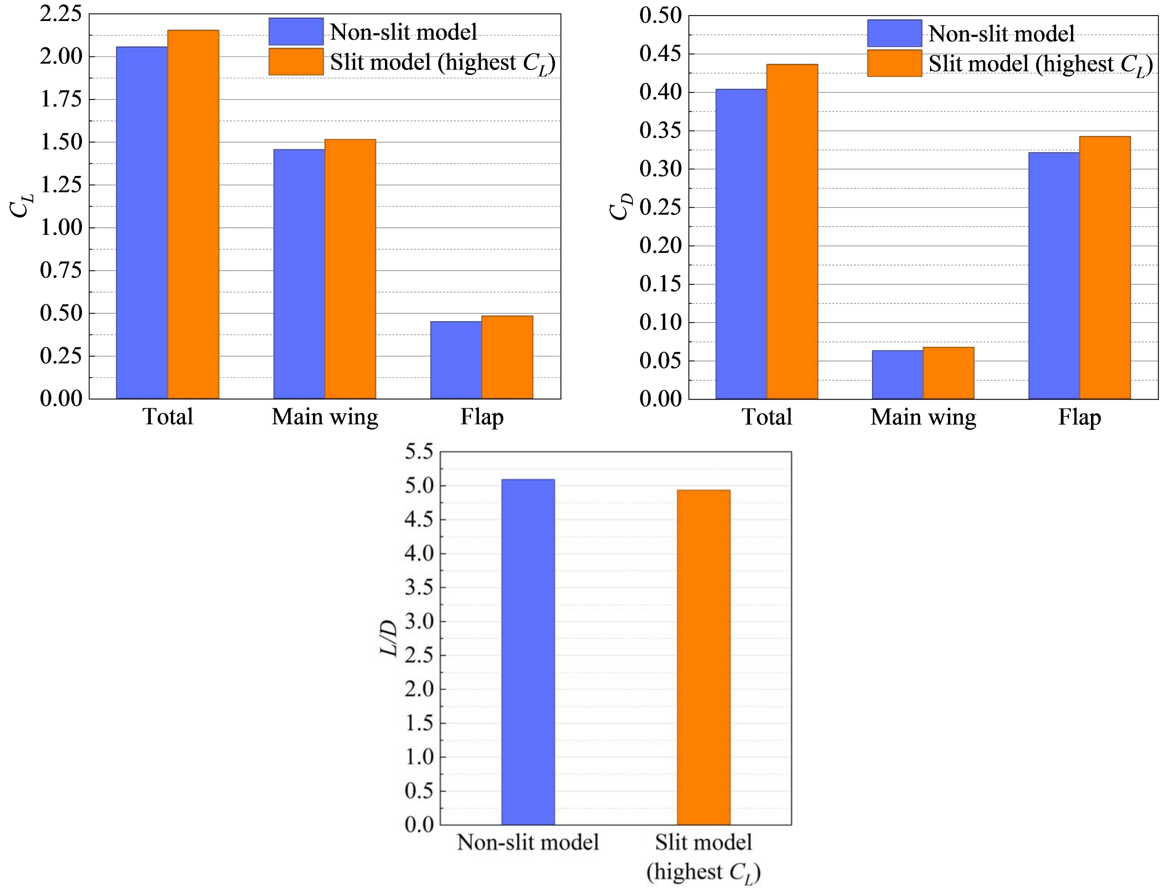

Figure 5: Aerodynamic performance of the baseline non-slit vs. the optimal slit configuration ($\lambda_\ell = 50\% c_{\text{flap}}$, $N = 8$, $\lambda_w = 1.0\% b_{\text{flap}}$). (a) Lift coefficient C_L; (b) Drag coefficient C_D; (c) Lift-to-drag ratio L/D. The slit configuration shows higher C_L and C_D than the non-slit, with moderate changes in L/D.

that differences in separation area and C_p distribution between the two models are far more pronounced on the flap's upper surface than on its lower surface. Accordingly, we focus on the flow over the flap's upper surface in each configuration.

3.1 Non-slit model

As shown in Fig. 3, a low-pressure region forms near the flap's leading edge due to the accelerated flow through the main wing-flap gap. However, the onset of separation shifts upstream between 25% and 55% of the flap span. Because the separation line shifts forward, the suction peak near the flap's leading edge is weakened. This raises the pressure both there and on the adjacent main-wing trailing edge, which in turn reduces lift. The surface streamlines indicate that wingtip vortices at both ends of the flap induce spanwise flow toward both the wingtip and the wing root. The boundary between these opposing spanwise flows forms a stagnation point, which contributes to the upstream shift of the separation line.

3.2 Slit model

Here, we investigate why the optimal slit configuration achieves a higher C_L than the baseline model. Figure 3 shows that the slit configuration sustains lower pressure on the flap's upper surface, indicating effective suppression of flow separation. Moreover, the low-pressure region extends from around the mid-chord of the main wing to the flap's trailing edge in the slit model — a region of suction that is absent in the baseline configuration. Figure 7 shows flow accelerating through the slits and emerging as a jet along the flap's upper surface from mid-chord to the trailing edge. This jet behaves like a virtual barrier, suppressing the spanwise movement of flow toward the wingtips and thereby reducing flow separation.

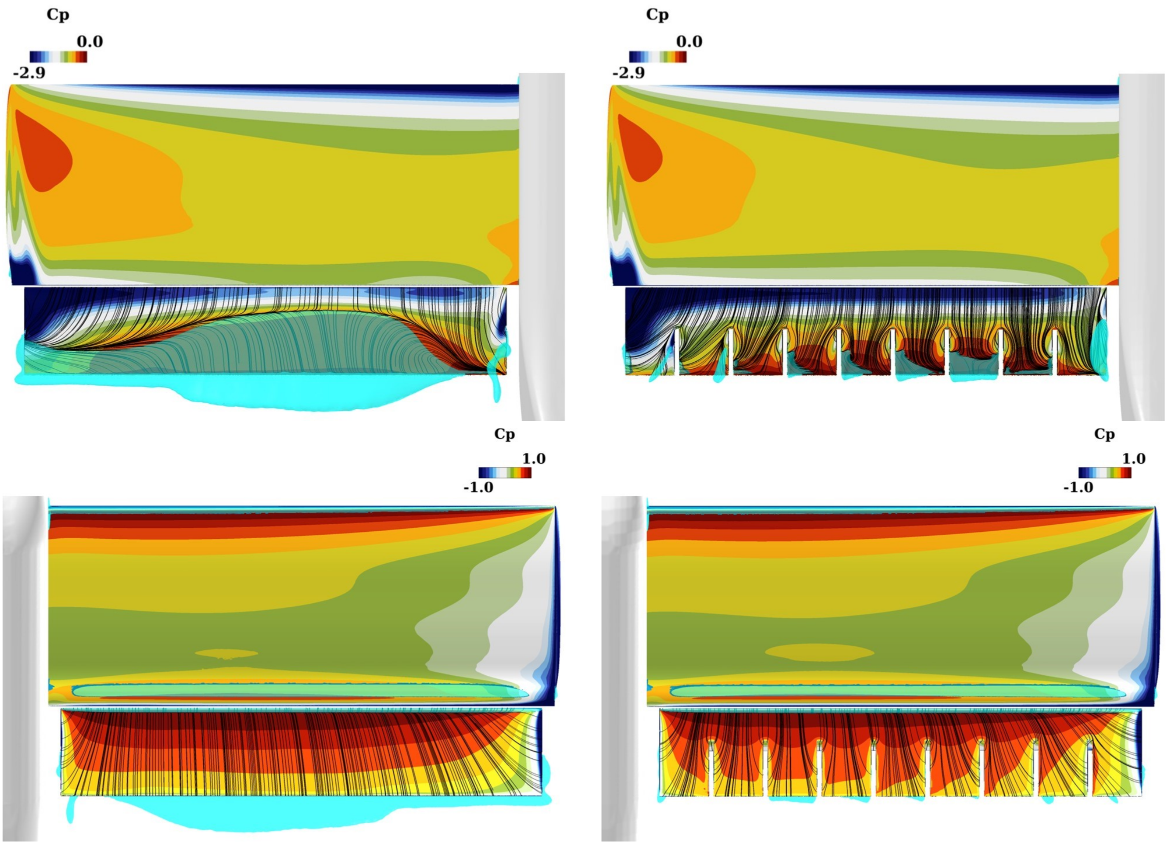

Figure 6: Surface pressure coefficient C_p contours, streamlines, and isosurfaces of streamwise velocity $u_{\mathrm{vel}} = 0$ (highlighted in translucent light-blue highlight on the contour plots) for the non-slit vs. slit configurations. (a) Upper surface – non-slit model, (b) Upper surface – slit model, (c) Lower surface – non-slit, (d) Lower surface – slit. The slit model shows a smaller separated region on the upper flap surface and different C_p distribution, especially near the flap leading edge, compared to the baseline.

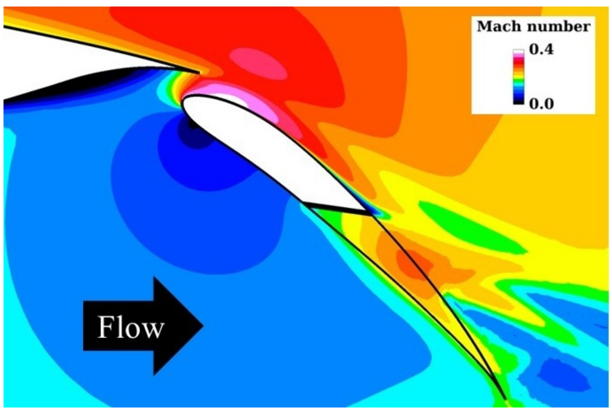

Figure 7: Mach number distribution on the x-z plane between the 4th and 5th flap segments from the wing root for the slit model ($\lambda_\ell = 50\% c_{\mathrm{flap}}$, $N = 8$, $\lambda_w = 1.0\% b_{\mathrm{flap}}$). This figure highlights the jet-like flow emerging through the slit and along the flap's upper surface.

These findings motivate a broader parametric study (presented next) to isolate the effects of each slit parameter.

Additionally, we discuss the factors responsible for variations in the size of the separation region along the spanwise direction, as shown in Fig. 3. Figure 8 shows the distribution of the z-direction velocity

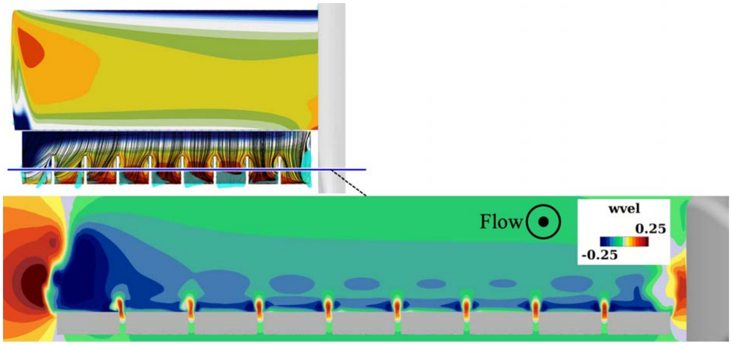

Figure 8: Upper panel: pressure/flow field on the flap's upper surface (slit model), reproduced from Fig. 3 with a blue line indicating a cross-section at 75% of the flap chord. Lower panel: distribution of vertical velocity w_{vel} in the corresponding y-z plane at 75% chord. Regions with suppressed separation exhibit a strong downward velocity component (dark blue), indicating vigorous downwash.

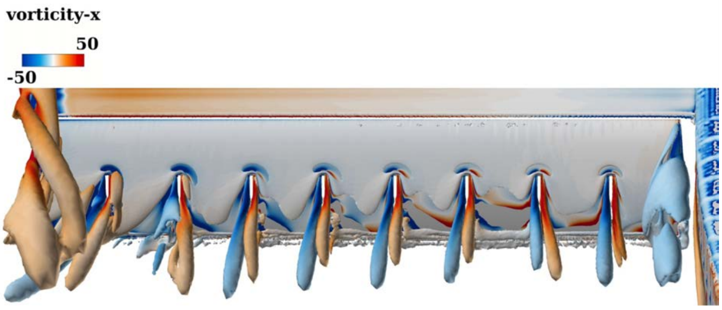

Figure 9: Isosurfaces of the Q-criterion (threshold $Q = 10$) for the slit model, colored by streamwise vorticity ω_x. Warm colors indicate clockwise-rotating vortices and cool colors counterclockwise. Vortices generated at the slits are drawn toward the wingtip vortices at the flap's ends, drifting either outboard or inboard; the 3rd flap segment (from the root) acts as a boundary between these two directions.

w_{vel} on the y-z cross-section at 75% of the flap chord. Figure 9 presents isosurfaces of the second invariant of the velocity gradient tensor, referred to as the Q-criterion [34], with a threshold value of $Q = 10$. As indicated in Fig. 8, regions where separation is suppressed exhibit a stronger downward velocity component than other areas. (Note that the isosurfaces of $u_{\text{vel}} = 0$ observed in the 1st, 8th, and 9th segments are not due to separation but are instead associated with wingtip vortices.) This behavior occurs because, as shown in Fig. 9, the downwash induced by the vortices generated at the slits pushes the separated flow back toward the surface. Furthermore, vortices formed at the slits tend to be drawn toward the wingtip vortices generated at the main wing and flap tips. As a result, they drift either outboard toward the wingtip or inboard toward the root, with the 3rd flap segment — where the tip vortices exert an influence — as a boundary between these two directions. Consequently, in the 4th-6th segments, the vortices on the root side move closer to each segment surface, creating broader downwash regions and stronger suppression of flow separation on the wing root side. In addition, at the wingtip and root-side segments, the downwash generated by the wingtip vortices originating from the main wing and flap tips suppresses overall separation. In contrast, in the 3rd segment, the vortices at both ends move away from the surface, leading to a more extensive separation region.

4. Results: parametric study

In this section, the effects of slit parameters on the C_L and the associated flow mechanisms are examined. Figure 10 presents the C_L results for the slit models with different parameter combinations. For all parameters, the peak occurs at $\lambda_\ell = 50\% c_{\text{flap}}$, $N = 8$, and $\lambda_w = 1.0\% b_{\text{flap}}$, while both larger and smaller

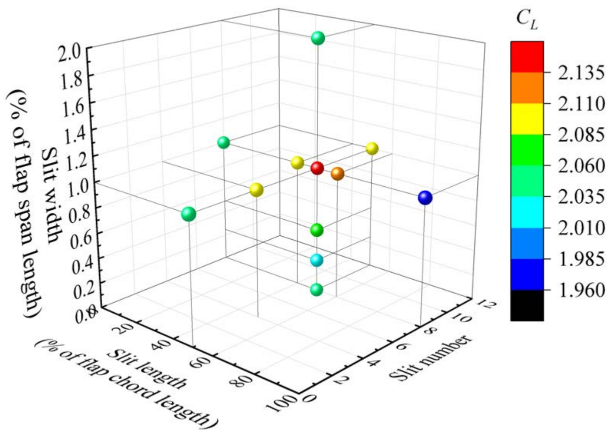

Figure 10: C_L results of the slit models with different parameter combinations. The maximum C_L is obtained at $\lambda_\ell = 50\% c_{\text{flap}}$, $N = 8$, and $\lambda_w = 1.0\% b_{\text{flap}}$, while either smaller or larger parameter settings result in reduced C_L.

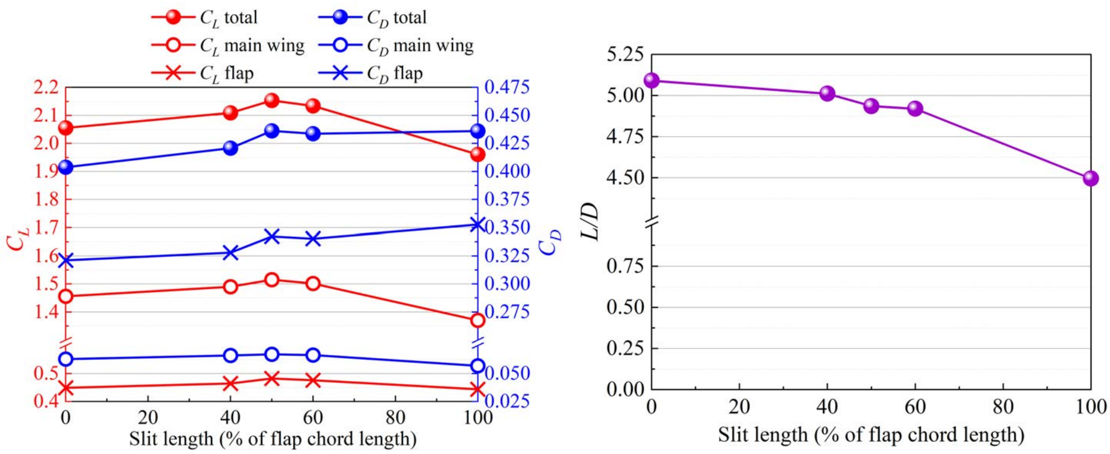

Figure 11: Variation of aerodynamic performance with slit length λ_ℓ. Here $\lambda_\ell = 0\% c_{\text{flap}}$ corresponds to the conventional (no-slit) flap. (a) Lift coefficient C_L and drag coefficient C_D; (b) Lift-to-drag ratio L/D. The configuration with $\lambda_\ell = 50\% c_{\text{flap}}$ yields the highest C_L and C_D. The variation in L/D is relatively small, except for the $\lambda_\ell = 100\% c_{\text{flap}}$ case.

parameter settings result in a decrease in C_L. This is because increasing λ_ℓ, N, or λ_w enhances separation control but simultaneously causes earlier pressure recovery upstream of the slits, raising the pressure on the flap's upper surface. These competing effects form a tradeoff, highlighting the need for careful parameter selection to achieve improvements in C_L.

4.1 Slit length λ_ℓ

Figure 11 shows the aerodynamic coefficients for different slit lengths (with $\lambda_\ell = 0\% c_{\text{flap}}$ representing the non-slit model). For λ_ℓ up to 50%, the overall C_L increases, whereas for λ_ℓ beyond 50%, it decreases. A similar trend is observed in the C_L of both the main wing and the flap. Relative to the $\lambda_\ell = 50\% c_{\text{flap}}$ case (the highest-C_L configuration), the reductions in C_L for the 40%, 60%, and 100% cases are:

- 40% slit model — overall configuration: −2.1%, main wing: −1.7%, flap: −3.7%
- 60% slit model — overall configuration: −0.9%, main wing: −0.9%, flap: −1.3%
- 100% slit model — overall configuration: −8.9%, main wing: −9.6%, flap: −7.9%

For C_D, the overall trend closely follows that of C_L, with the exception of the $\lambda_\ell = 100\% c_{\text{flap}}$ configuration.

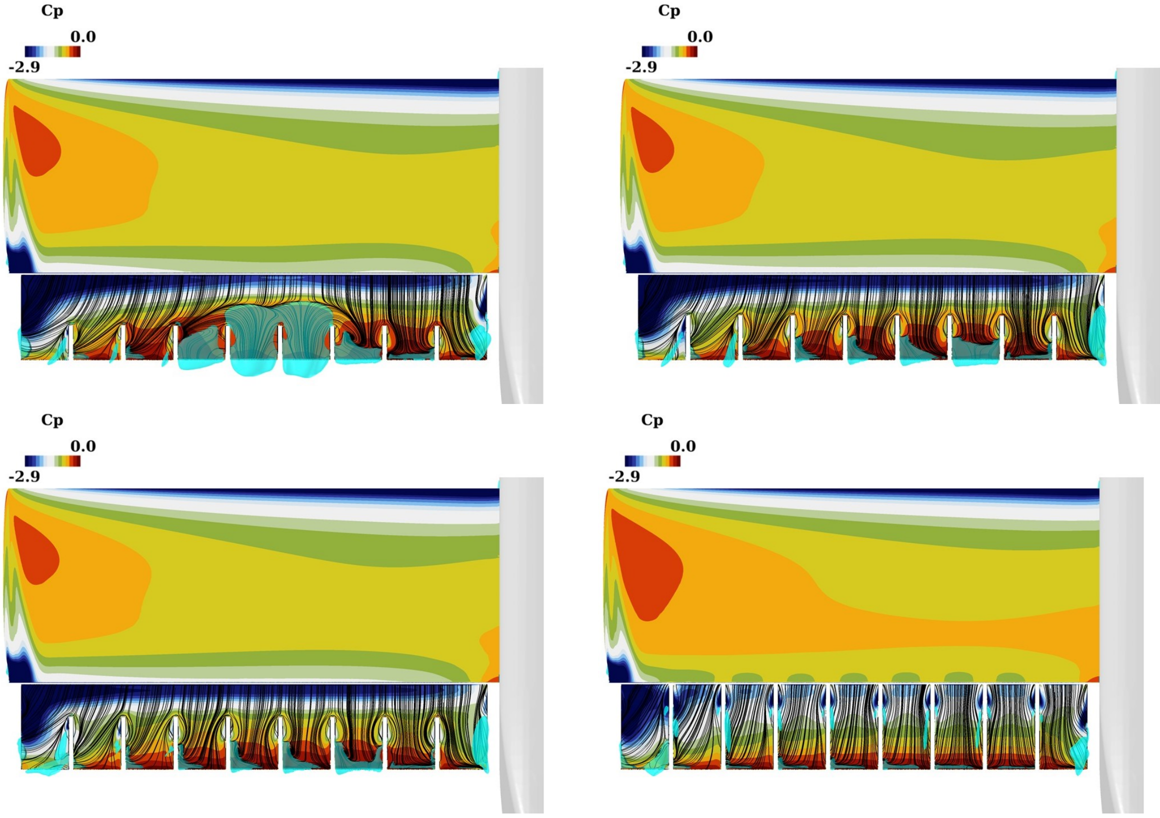

Figure 12: Upper-surface pressure distribution C_p, streamlines, and isosurfaces of streamwise velocity $u_{\text{vel}} = 0$ for various slit lengths. (a) $\lambda_\ell = 40\%c_{\text{flap}}$ (short slit), (b) $\lambda_\ell = 50\%c_{\text{flap}}$ (moderate slit), (c) $\lambda_\ell = 60\%c_{\text{flap}}$, (d) $\lambda_\ell = 100\%c_{\text{flap}}$ (full-chord slit). Comparing (a)–(d) illustrates how increasing λ_ℓ first improves then degrades the flow: the $\lambda_\ell = 50\%c_{\text{flap}}$ case (b) has the best separation control with minimal pressure penalty, whereas $\lambda_\ell = 40\%c_{\text{flap}}$ has more separation and $\lambda_\ell = 100\%c_{\text{flap}}$ shows high pressure near the leading edge despite minimal separation.

As a result, the variation in L/D with slit length is relatively small across the tested cases. In $\lambda_\ell = 100\%c_{\text{flap}}$ case, C_D increases further because streamwise vortices form earlier at the slit corners and intensify as they develop downstream.

To clarify these C_L variations with the underlying flow structures, Fig. 12 presents the upper-surface C_p distributions, surface streamlines, and separation regions for each configuration. Furthermore, Figs. 13 and 14 visualize w_{vel} and streamwise vorticity ω_x distributions in the y-z plane at 75% of the flap chord for each model. The following discussion focuses on the factors leading to the reduction in C_L for the $\lambda_\ell = 40\%$, 60%, and $100\%c_{\text{flap}}$ slit models relative to the $\lambda_\ell = 50\%c_{\text{flap}}$ case.

4.1.1 $\lambda_\ell = 40\%c_{\textbf{flap}}$

Figure 4.1 indicates that in the $\lambda_\ell = 40\%c_{\text{flap}}$ case, the flap's leading-edge pressure is higher over a spanwise band of about 30–55% span (compared to the $\lambda_\ell = 50\%c_{\text{flap}}$ case). This localized pressure rise extends to the main wing's trailing edge, causing a reduction in overall C_L.

The partial pressure recovery at the flap leading edge originates from flow separation occurring at approximately 40% of the chord on the fourth and fifth flap segments from the wing root. As indicated by the surface streamlines, this separation occurs because the flow splits and travels toward both ends of the flap before the high-speed slit jet can develop and halt this spanwise movement.

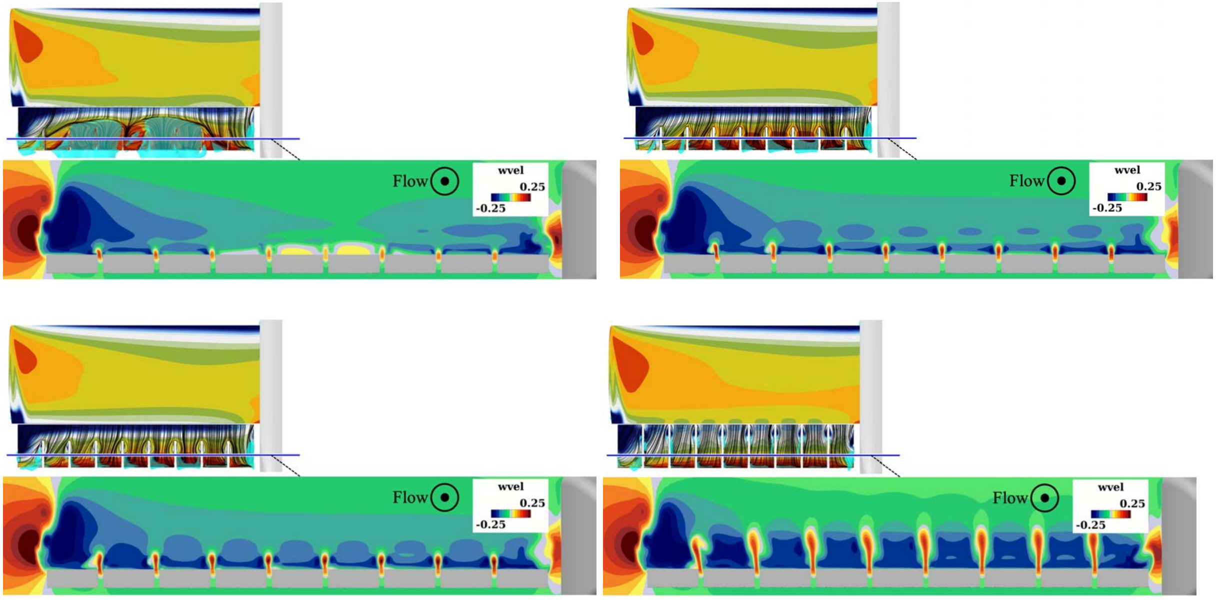

Figure 13: Distribution of z-direction velocity w_{vel} in the y-z cross-section at the 75% position of the flap chord length (the upper panel is reproduced from Fig. 12, and the blue line newly added here indicates this 75% position). (a) $\lambda_\ell = 40\%c_{\mathrm{flap}}$ (short slit), (b) $\lambda_\ell = 50\%c_{\mathrm{flap}}$ (moderate slit), (c) $\lambda_\ell = 60\%c_{\mathrm{flap}}$, (d) $\lambda_\ell = 100\%c_{\mathrm{flap}}$ (full-chord slit). Comparing (a)–(d) illustrates that the downward velocity near the upper surface of each segment becomes greater as the slit length increases.

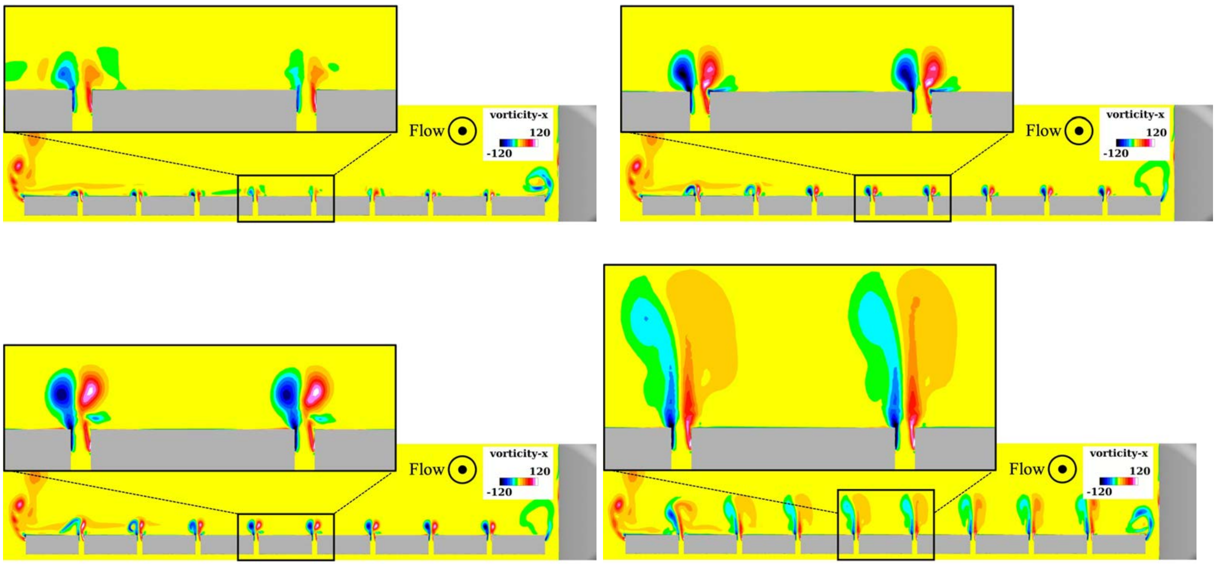

Figure 14: Distribution of x-direction vorticity ω_x in the y-z cross-section at the 75% position of the flap chord length. (a) $\lambda_\ell = 40\%c_{\mathrm{flap}}$ (short slit), (b) $\lambda_\ell = 50\%c_{\mathrm{flap}}$ (moderate slit), (c) $\lambda_\ell = 60\%c_{\mathrm{flap}}$, (d) $\lambda_\ell = 100\%c_{\mathrm{flap}}$ (full-chord slit). Warm colors represent clockwise vortex rotation, while cool colors indicate counterclockwise rotation (yellow is neutral). For $\lambda_\ell \leq 60\%c_{\mathrm{flap}}$, the intensity of the wingtip vortices for each flap strengthens as the slit length increases. For the full-chord slit, the vortices are weaker in intensity but larger in size than those in the other models.

4.1.2 $\lambda_\ell = 60\%c_{\mathrm{flap}}$

In the $\lambda_\ell = 60\%c_{\mathrm{flap}}$ case (Fig. 4.1), the separated region on the flap is further reduced compared to $\lambda_\ell = 50\%c_{\mathrm{flap}}$, which lowers the pressure over most of the flap's upper surface. However, this configuration also experiences an earlier pressure rise starting near the flap's leading edge, which confines the suction peak to a smaller region. Consequently, the high-suction area contributing to lift is reduced, and the net C_L is lower than in the $\lambda_\ell = 50\% c_{\text{flap}}$ case. This premature pressure recovery also affects the main wing: the pressure near the trailing edge of the main wing is higher than in the optimal case, contributing to the overall C_L reduction.

This enhanced separation suppression can be explained by the flow structure: Fig. 4.1.1 shows that the $\lambda_\ell = 60\% c_{\text{flap}}$ case produces a stronger downward velocity near the flap's upper surface compared to the 50% case. This downward motion pushes the incipient separated flow back to the surface. This is because the onset location of the tip vortices generated at the slits is positioned further upstream, and their vortex strength exceeds that of the $\lambda_\ell = 50\% c_{\text{flap}}$ case (Figs. 4.1.1 and 4.1.1).

4.1.3 $\lambda_\ell = 100\% c_{\text{flap}}$

With $\lambda_\ell = 100\% c_{\text{flap}}$ (a full-chord slit, Fig. 4.1), flow separation on the flap is almost entirely eliminated, resulting in very low pressure over the majority of the flap. However, the pressure near the flap's leading edge rises significantly — higher than in any other configuration — which leads to the lowest C_L among all cases. In terms of vortical structures, this full-chord slit generates tip vortices that are weaker in intensity but more broadly distributed over each segment (Fig. 4.1.1), producing a uniform downwash across the entire flap segment. This adverse effect arises because each flap segment behaves like an isolated wing: flow wraps around the segment's side edges and is drawn inward along the leading-edge corners, interfering with the main-wing gap flow. The gap flow is thus weakened, causing a loss of suction (i.e. higher pressure) at the flap's leading edge.

These observations underscore the role of spanwise and vertical flow in determining separation characteristics across slit configurations. In the $\lambda_\ell = 40\% c_{\text{flap}}$ model, flow begins to turn spanwise toward the flap edges before the slit jet develops, leading to premature separation. In contrast, the slit jet in the $\lambda_\ell = 50\% c_{\text{flap}}$ model blocks most of this spanwise flow, delaying separation. While this broad downwash suppresses separation effectively for $\lambda_\ell = 100\% c_{\text{flap}}$ model, it comes at the cost of a greatly diminished suction peak at the leading edge. These observations indicate that $\lambda_\ell = 50\% c_{\text{flap}}$ provides the best balance: it is long enough to substantially suppress flow separation, yet short enough to avoid excessive pressure recovery near the flap's leading edge. This balance results in the highest C_L among the cases studied. Having examined slit length, we next assess how varying the number of slits and slit width influences the aerodynamics.

4.2 Slit number N

Figure 15 indicates the variation of the aerodynamic coefficients with the number of slits N. The configuration with $N = 8$ achieves the highest C_L, while both fewer and greater numbers of slits result in reduced C_L. This trend is consistent for the C_L of both the main wing and the flap. The percentage reductions in C_L for the $N = 4$ and $N = 12$ slit models, relative to the $N = 8$ configuration, are as follows:

- $N = 4$ — overall configuration: −3.1%, main wing: −2.7%, flap: −4.6%
- $N = 12$ — overall configuration: −2.9%, main wing: −2.1%, flap: −5.4%

C_D follows nearly the same trend as C_L, and L/D varies by only about ±2.4% across these cases.

To investigate the factors contributing to the C_L variations associated with changes in the number of slits, Fig. 16 visualizes the upper-surface C_p distributions, surface streamlines, and separation regions of each model. The following discussion examines the mechanisms responsible for the reduction in C_L observed in the $N = 4$ and $N = 12$ slit models compared with the $N = 8$ configuration.

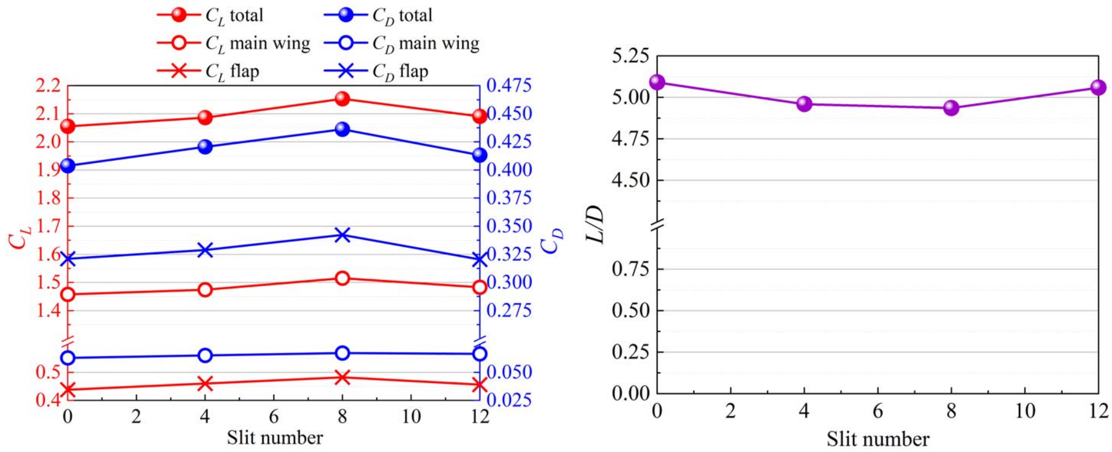

Figure 15: Variation of aerodynamic performance with slit number N. (Here $N = 0$ corresponds to the no-slit flap.) (a) C_L and C_D; (b) L/D. The configuration with $N = 8$ yields the highest C_L and C_D, while both fewer and more slits result in lower lift and drag. The variation in L/D is relatively small.

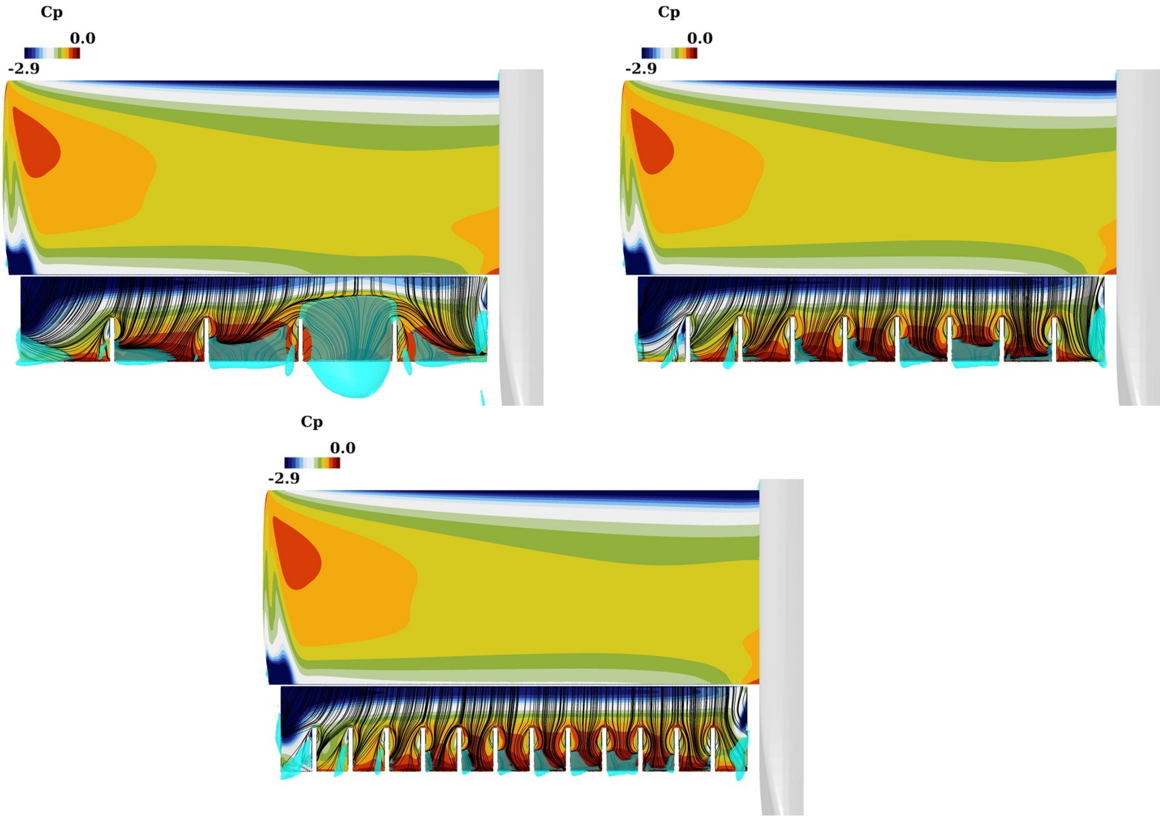

Figure 16: Upper-surface C_p distribution, streamlines, and isosurfaces of $u_{\text{vel}} = 0$ for various slit numbers. (a) $N = 4$, (b) $N = 8$, (c) $N = 12$. For $N = 8$, separation control is optimal while the pressure increase is minimal. In contrast, with $N = 4$ a larger separated region appears, and with $N = 12$ the separation is as well-controlled as in $N = 8$ but the pressure recovery occurs more rapidly on the flap, leading to higher pressure near the leading edge.

4.2.1 N=4

Figure 4.2 shows that the $N = 4$ slit model exhibits higher pressure near the flap's leading edge (across 15–45% of the span), along with increased pressure at the main wing's trailing edge, compared to the

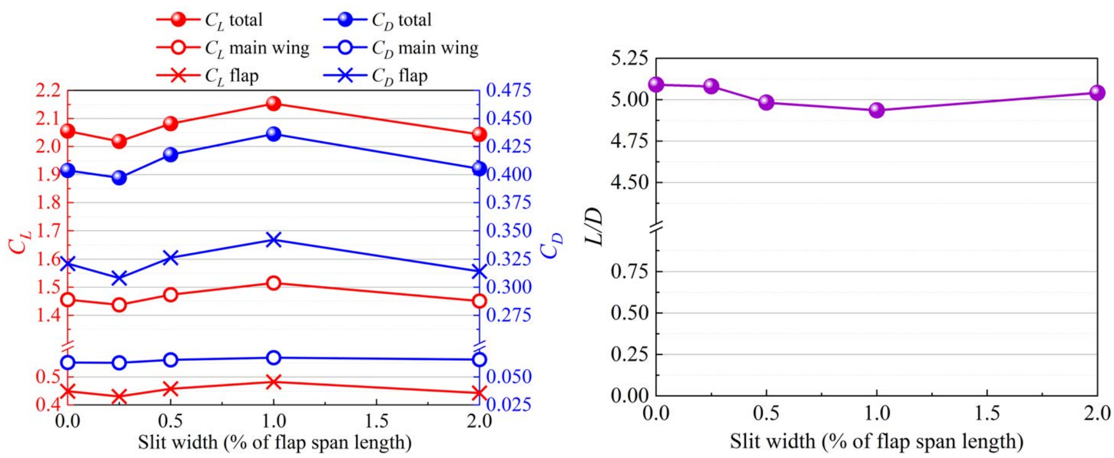

Figure 17: Variation of aerodynamic performance with slit width λ_w. (Here $\lambda_w = 0.0 b_{\text{flap}}$ corresponds to the no-slit flap.) (a) C_L and C_D; (b) L/D. The configuration with $\lambda_w = 1.0\% b_{\text{flap}}$ yields the highest C_L and C_D, while both narrower and wider slit widths result in lower lift and drag. The change in L/D due to slit width remains small.

$N = 8$ case. This pressure rise leads to a lower overall C_L relative to the $N = 8$ configuration.

The elevated pressure at the flap leading edge originates from flow separation at approximately 30% of the flap chord on the 2nd flap segment from the wing root. Surface streamlines suggest that the wider spacing between slits (in the $N = 4$ model) allows more spanwise flow over each flap segment, promoting the observed separation.

4.2.2 N=12

Figure 4.2 shows that the $N = 12$ model has an earlier pressure recovery on the flap's upper surface compared to the $N = 8$ case. As a result, the low-pressure region near the flap leading edge is reduced, leading to higher pressure at the trailing edge of the main wing.

This effect corresponds to the adverse mechanism described in Section 4.1.2, namely the accelerated pressure recovery upstream of the slits, which extends over a broader region as the number of slits increases. In contrast, the separation region shows no significant change between $N = 8$ and $N = 12$, suggesting that around eight slits are sufficient to eliminate most separation on the flap. Adding more slits beyond this number yields no further separation benefit and only incurs the penalty of earlier pressure recovery.

These observations show how the number of slits influences spanwise flow control. When $N = 4$, the larger flap segments between slits encourage spanwise flow, leading to earlier separation. With $N = 8$, jet flows interrupt spanwise flow over shorter intervals, delaying separation. Increasing to $N = 12$ does not significantly improve separation suppression compared with $N = 8$. However, the faster pressure recovery upstream of the slits spreads over a wider area, raising the pressure near the flap leading edge. Thus, in flap design, N should be set to the minimum needed to prevent flow separation, while avoiding excessive pressure recovery that could reduce lift performance.

4.3 Slit width λ_w

Figure 17 presents the aerodynamic coefficients for different slit widths (with $\lambda_w = 0.0\% b_{\text{flap}}$ corresponding to the non-slit model). The results show that C_L peaks at $\lambda_w = 1.0\% b_{\text{flap}}$, and that both smaller and larger slit widths yield lower C_L. The percentage reductions in C_L relative to the $\lambda_w = 1.0\% b_{\text{flap}}$ case are:

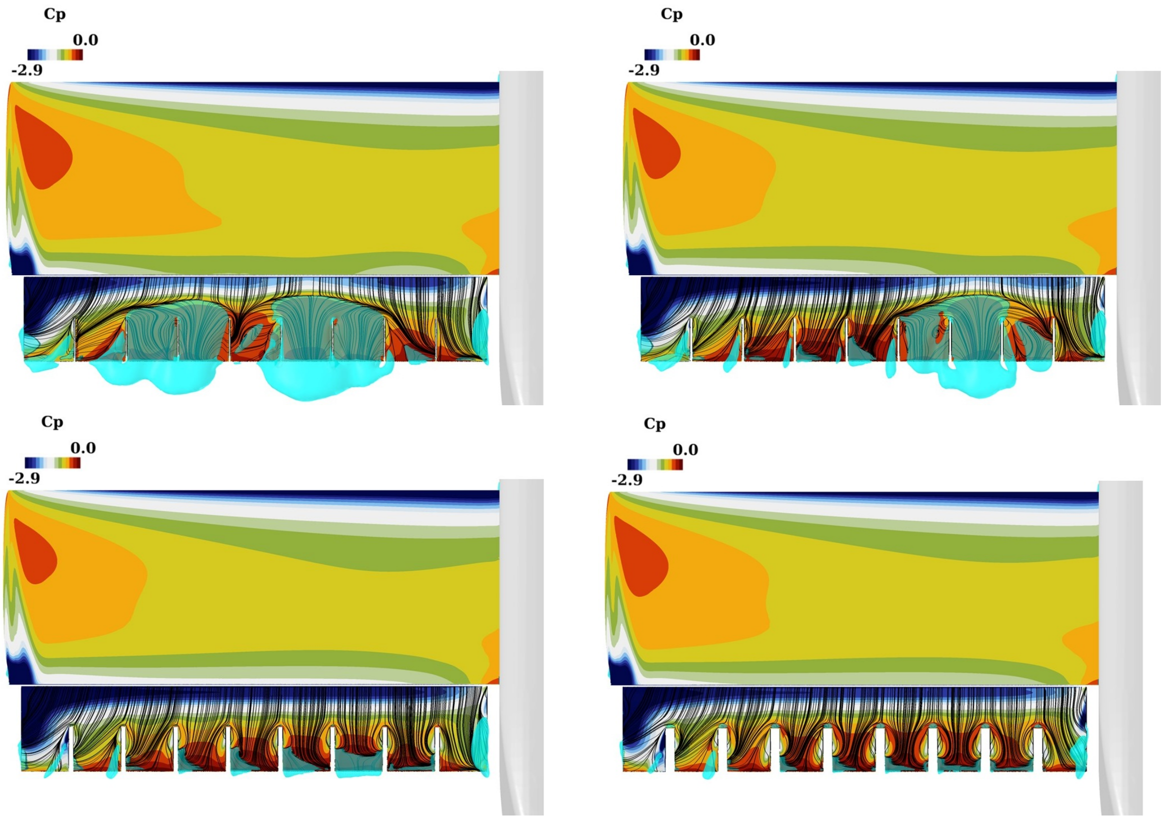

Figure 18: Upper-surface C_p distribution, streamlines, and isosurfaces of $u_{\text{vel}} = 0$ for various slit widths. (a) $\lambda_w = 0.25\% b_{\text{flap}}$, (b) $\lambda_w = 0.5\% b_{\text{flap}}$, (c) $\lambda_w = 1.0\% b_{\text{flap}}$, (d) $\lambda_w = 2.0\% b_{\text{flap}}$. Comparing (a)–(d) illustrates how increasing λ_w first improves then degrades the flow: the $\lambda_w = 1.0\% b_{\text{flap}}$ case (c) has the best separation control with minimal pressure penalty, whereas $\lambda_w = 0.25\% b_{\text{flap}}$ has more separation and $\lambda_w = 2.0\% b_{\text{flap}}$ shows high pressure near the leading edge despite minimal separation.

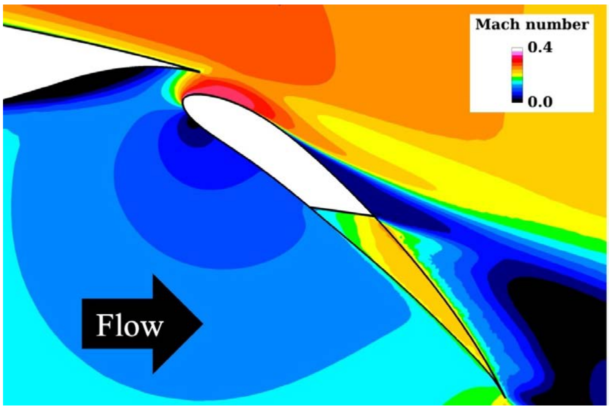

Figure 19: Mach number distribution on the x-z plane between the 4th and 5th flap segments from the wing root for the $\lambda_w = 0.25\% b_{\text{flap}}$ slit model. The flow accelerated between the slits is not effectively ejected onto the flap's upper surface due to the narrow slit width, resulting in weaker separation suppression.

- $\lambda_w = 0.25\% b_{\text{flap}}$ — overall configuration: −6.3%, main wing: −5.2%, flap: −11%
- $\lambda_w = 0.5\% b_{\text{flap}}$ — overall configuration: −3.3%, main wing: −2.8%, flap: −5.1%
- $\lambda_w = 2.0\% b_{\text{flap}}$ — overall configuration: −5.1%, main wing: −4.2%, flap: −8.2%

C_D exhibits a trend similar to C_L, and the variation in L/D with slit width is only about 2.8%.

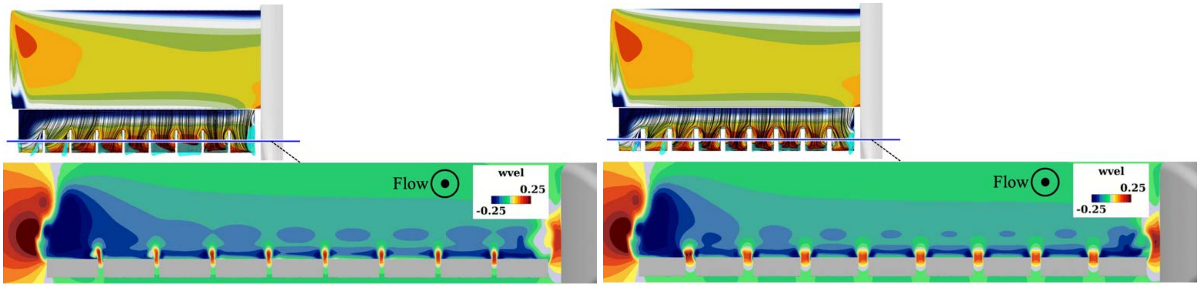

Figure 20: Distribution of w_{vel} in the y-z cross-section at the 75% flap chord position (the upper panel is adapted from Fig. 18, with the blue line newly added here to indicate this position). (a) $\lambda_w = 1.0\% b_{\text{flap}}$, (b) $\lambda_w = 2.0\% b_{\text{flap}}$. Comparing (a) and (b) illustrates that a wider slit width results in a greater downward velocity on the upper surface of each flap segment.

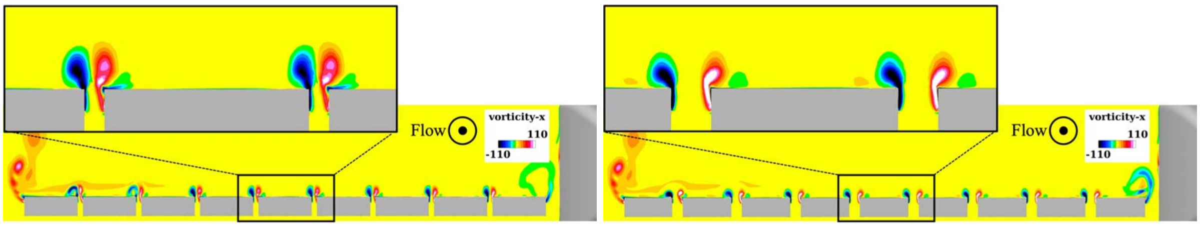

Figure 21: Distribution of ω_x in the y-z cross-section at the 75% position of the flap chord length. (a) $\lambda_w = 1.0\% b_{\text{flap}}$, (b) $\lambda_w = 2.0\% b_{\text{flap}}$. Warm colors represent clockwise vortex rotation, while cool colors indicate counterclockwise rotation (yellow is neutral). Comparing (a) and (b), a wider slit width results in a stronger tip vortex for each flap segment.

To examine the mechanisms underlying these C_L variations, Fig. 18 shows the upper-surface C_p distributions, surface streamlines, and separation regions for each configuration. We focus next on explaining why the $\lambda_w = 0.25\%$, 0.5%, and $2.0\% b_{\text{flap}}$ cases achieve lower C_L than the optimal $\lambda_w = 1.0\% b_{\text{flap}}$ case.

4.3.1 $\lambda_w = 0.25\% b_{\textbf{flap}}$

As shown in Fig. 4.3, the $\lambda_w = 0.25\% b_{\text{flap}}$ model exhibits higher pressure in the flap leading-edge region spanning 20–75% of the span, together with increased pressure near the trailing edge of the main wing relative to the $\lambda_w = 1.0\% b_{\text{flap}}$ case. This rise in pressure reduces the overall C_L. This elevated leading-edge pressure originates from flow separation between ~ 30–50% of the flap chord on the 3rd, 4th, 6th, and 7th flap segments.

To understand why separation is not as effectively suppressed as in the $\lambda_w = 1.0\% b_{\text{flap}}$ case, Fig. 19 shows the Mach number distribution in the x-z plane through the slit (at the same spanwise position as in Fig. 7). Because the slit is very narrow, the accelerated flow through it does not form an effective jet along the flap's upper surface. As a result, spanwise flow over the flap is not suppressed, leading to premature separation.

4.3.2 $\lambda_w = 0.5\% b_{\textbf{flap}}$

As shown in Fig 4.3, in the $\lambda_w = 0.5\% b_{\text{flap}}$ case a separation on the 3rd segment from the wing root raises the flap's leading-edge pressure over 10–40% of the span (compared to the $\lambda_w = 1.0\% b_{\text{flap}}$ case). A corresponding rise in pressure is also observed in the same spanwise range near the trailing edge of the main wing. For $\lambda_w = 0.5\% b_{\text{flap}}$, the flow passes through the slits more easily than in the $\lambda_w = 0.25\% b_{\text{flap}}$

case, so separation is suppressed more effectively, though still not as well as in the optimal $\lambda_w = 1.0\%b_{\text{flap}}$ case.

4.3.3 $\lambda_w = 2.0\%b_{\textbf{flap}}$

Figure 4.3 shows that the $\lambda_w = 2.0\%b_{\text{flap}}$ configuration has a substantially smaller separated-flow region compared to the $\lambda_w = 1.0\%b_{\text{flap}}$ case. However, the pressure recovers earlier along the flap, which narrows the low-pressure region near the flap's leading edge and increases the pressure at the main wing's trailing edge. This behavior reflects the same detrimental mechanism discussed in Sections 4.1.2 and 4.2.2: as slit width increases, premature pressure recovery (upstream of the slits) becomes more pronounced.

To further examine the mechanism by which larger slit widths suppress separation, Figs. 20 and 21 show cross-sectional distributions of w_{vel} and ω_x (in a y-z plane at 75% of the flap chord) for the $\lambda_w = 1.0\%b_{\text{flap}}$ and $\lambda_w = 2.0\%b_{\text{flap}}$ models. As Fig. 4.3 shows, the $\lambda_w = 2.0\%b_{\text{flap}}$ case produces a more uniformly distributed downwash over each flap segment compared to the $\lambda_w = 1.0\%b_{\text{flap}}$ case. This occurs because with a wider slit, the counter-rotating vortex pairs remain separate and retain their strength. In the $\lambda_w = 1.0\%b_{\text{flap}}$ configuration, by contrast, those vortices interact and weaken each other (Fig. 21). The larger $\lambda_w = 2.0\%b_{\text{flap}}$ vortices further enhance separation suppression, but they also induce a broader region of accelerated pressure recovery upstream of the slits, which raises the pressure at the flap's leading edge. Consequently, $\lambda_w = 1.0\%b_{\text{flap}}$ provides the best balance: it strongly suppresses separation without causing excessive leading-edge pressure.

5. Conclusions

This study numerically examined the aerodynamic impact of adding multiple chordwise slits near the trailing edge of a slotted flap, as well as the effects of varying key slit parameters. To evaluate slit effectiveness, we compared a conventional flap without slits to the configuration identified in a parametric study as achieving the highest C_L. The slit length, number, and width were systematically varied to assess their influence on lift and flow characteristics.

Results indicate that, compared with the non-slit flap, the slit configuration reduced flow separation on the upper surface and increased the suction peak near the flap's leading edge, producing a 4.7% lift enhancement in the optimal case. Jet-like flows emerging from the slits act as virtual barriers, suppressing spanwise crossflow and further limiting separation. The parametric effects of slit geometry on lift performance, along with the associated physical mechanisms, are summarized below:

- **Slit length:** A slit length equal to 50% of the flap chord produced the highest C_L in the present model. Increasing the slit length strengthened and enlarged the streamwise vortices generated at the slits, inducing stronger downward velocity over each segment and suppressing flow separation. However, longer slits also promoted earlier pressure recovery upstream, raising the pressure near the flap's leading edge.
- **Slit number:** Eight slits yielded the highest C_L. Adding more slits reduced the spanwise width of each segment, limiting crossflow and further suppressing separation. Beyond about eight slits, however, the benefits saturate. Adding more slits only broadens the region of early pressure recovery, which in turn raises the pressure near the flap's leading edge.
- **Slit width:** A slit width equal to 1.0% of the flap span produced the highest C_L. Wider slits weakened the interaction between counter-rotating vortex pairs, allowing each vortex to intensify. This generated stronger downwash over each segment and suppressed separation. At the same time, wider slits expanded the region of early pressure recovery, raising pressure near the leading edge.

The effectiveness of chordwise slits is governed by a tradeoff between beneficial and detrimental effects.

Maximizing C_L requires careful tuning of the slit parameters for a given flap geometry. While the slitted flap achieved a $\sim$ 4.7% lift increase, it also incurred a moderate drag penalty (about 8% higher C_D, yielding a 3% drop in L/D). This tradeoff highlights the need to balance lift gains against potential drag costs in design. These findings were obtained at a representative landing angle of attack (8°). Future studies should examine whether the optimal slit parameters remain effective at different flight conditions or flap deflections. In future work, we will extend this concept to flaps with spanwise-varying deflection angles. The aim is to minimize C_D during takeoff and maximize C_L during landing by optimally adjusting each segment's deflection angle. In addition to aerodynamic benefits, the chordwise-slit approach could potentially avoid the weight penalties of multi-slotted flaps (though structural feasibility remains to be studied). To this end, the practicality of implementing segmented flaps with acceptable structural and mechanical complexity should also be addressed in future work.

Acknowledgments

The CFD visualizations in this study were generated using FieldView 2022, supplied by FieldView CFD, Inc. through its University Partners Program.

References

[1] Antonio Filippone. Cruise altitude flexibility of jet transport aircraft. *Aerospace Science and Technology*, 14(4):283–294, 2010.

[2] P Garner, P Meredith, and R Stoner. Areas for future cfd development as illustrated by transport aircraft applications. In *10th Computational Fluid Dynamics Conference*, page 1527, 1991.

[3] CP Van Dam. The aerodynamic design of multi-element high-lift systems for transport airplanes. *Progress in Aerospace sciences*, 38(2):101–144, 2002.

[4] Kade Stephen Aley, Tufan Kumar Guha, and Rajan Kumar. Active flow control of a high-lift supercritical airfoil with microjet actuators. *AIAA Journal*, 58(5):2053–2069, 2020.

[5] HuBing Chu, BinQian Zhang, YingChun Chen, YaLin Li, and Jun Mao. Investigation of micro vortex generators on controlling flow separation over scch high-lift configuration. *Science China Technological Sciences*, 55:1943–1953, 2012.

[6] Harry L Morgan Jr and John W Paulson Jr. Low-speed aerodynamic performance of a high-aspect-ratio supercritical-wing transport model equipped with full-span slat and part-span double-slotted flaps. Technical report, 1979.

[7] Lysle P Parlett. *Wind-Tunnel Investigation of an External-Flow Jet-Flap Transport Configuration Having Full-Span Triple-Slotted Flaps*. National Aeronautics and Space Administration, 1971.

[8] John C Lin. Review of research on low-profile vortex generators to control boundary-layer separation. *Progress in aerospace sciences*, 38(4-5):389–420, 2002.

[9] Brian Allan, Chung-Sheng Yao, and John Lin. Numerical simulations of vortex generator vanes and jets on a flat plate. In *1st Flow Control Conference*, page 3160, 2002.

[10] Jesse Little, Munetake Nishihara, Igor Adamovich, and Mo Samimy. High-lift airfoil trailing edge separation control using a single dielectric barrier discharge plasma actuator. *Experiments in fluids*, 48:521–537, 2010.

[11] Zhengyu Zuo and Xin Zhang. Flow control over a two-element airfoil using a dielectric-barrier-discharge plasma actuator. *AIAA Journal*, pages 1–11, 2025.

[12] Qiangqiang Sun, Faycal Bahri, Mark Jabbal, Wit Stryczniewicz, Richard Jefferson-Loveday, Bruno Stefes, and Alexander Büscher. Suppression of flow separation of a high-lift wing with active flow control. *Aerospace Science and Technology*, page 110017, 2025.

[13] Gang Wang and Binqian Zhang. Numerical study on technical and conceptual improvements to a civil aircraft trailing-edge flap using passive/active flow control. *Engineering Applications of Computational Fluid Mechanics*, 15(1):1362–1391, 2021.

[14] Peter KC Rudolph. Airfoil flap assembly with flap track member, March 6 1984. US Patent

4,434,959.

[15] Seung-Hee Ko, Jae-Sung Bae, and Jin-Ho Rho. Development of a morphing flap using shape memory alloy actuators: the aerodynamic characteristics of a morphing flap. *Smart materials and structures*, 23(7):074015, 2014.

[16] James HS Fincham and Michael Ian Friswell. Aerodynamic optimisation of a camber morphing aerofoil. *Aerospace Science and technology*, 43:245–255, 2015.

[17] Keita Kambayashi, Nozomu Kogiso, Takayuki Yamada, Kazuhiro Izui, Shinji Nishiwaki, and Masato Tamayama. Multiobjective topology optimization for a multi-layered morphing flap considering multiple flight conditions. *Transactions of the Japan Society for Aeronautical and Space Sciences*, 63(3):90–100, 2020.

[18] Kazuhisa Chiba, Tatsuro Komatsu, and Takeshi Ito. Aerodynamic efficacy of adding yaw-wise rotational degree of freedom to an airplane flap. *Aerospace Systems*, 3:207–217, 2020.

[19] Kazuhisa Chiba and Masahiro Kanazaki. Feedback-circulating design space exploration by multi-sampling kriging model: Exploitation for the lift rise by an aircraft flap with yaw-wise rotation. In *Proceedings of the 2023 7th International Conference on Intelligent Systems, Metaheuristics & Swarm Intelligence*, pages 119–123, 2023.

[20] Piper Sigrest and Daniel J Inman. Avian whiffling-inspired gaps provide an alternative method for roll control. *Bioinspiration & Biomimetics*, 17(4):046014, 2022.

[21] Piper Sigrest, Ella Wu, and Daniel J Inman. Energy considerations and flow fields over whiffling-inspired wings. *Bioinspiration & Biomimetics*, 18(4):046007, 2023.

[22] Robert A. McDonald and James R. Gloudemans. Open Vehicle Sketch Pad: An open source parametric geometry and analysis tool for conceptual aircraft design. In *AIAA Paper-2022-0004 on the AIAA SciTech 2022 Forum*, page 0004. AIAA, 2022.

[23] Mitsuhiro Murayama, Yuzuru Yokokawa, Kazuomi Yamamoto, Hiroki Ura, Taro Imamura, Tohru Hirai, Yasushi Ito, Dongyoun Kwak, Hiroshi Kobayashi, and Shigemi Shindo. Investigation of noise generation from bluff flap side-edge of a high-lift wing model. *Transactions of the Japan Society for Aeronautical and Space Sciences, Aerospace Technology Japan*, 12(APISAT-2013):a9–a16, 2014.

[24] Christopher L Rumsey, Jeffrey P Slotnick, Michael Long, Robert A Stuever, and TR Wayman. Summary of the first aiaa cfd high-lift prediction workshop. *Journal of Aircraft*, 48(6):2068–2079, 2011.

[25] Y. Ito and K. Nakahashi. Direct Surface Triangulation Using Stereolithography Data. *AIAA Journal*, 40(3):490–496, 2002.

[26] Y. Ito, A. M. Shih, and B. K. Soni. Hybrid Mesh Generation with Embedded Surfaces Using a Multiple Marching Direction Approach. *International Journal for Numerical Methods in Fluids*, 67(1):1–7, 2011.

[27] A. Hashimoto, K. Murakami, T. Aoyama, K. Ishiko, M. Hishida, M. Sakashita, and P. R. Lahur. Toward the Fastest Unstructured CFD Code “FaSTAR”. In *AIAA Paper-2012-1075 on the 50th AIAA Aerospace Sciences Meeting*, page 1075. AIAA, 2012.

[28] B. van Leer. Towards the Ultimate Conservative Differences Scheme V. A Second Order Sequel to Godunov’s Method. *Journal of Computational Physics*, 32(1):101–136, 1979.

[29] M. Hishida, A. Hashimoto, K. Murakami, and T. Aoyama. A New Slope Limiter for Fast Unstructured CFD Solver FaSTAR. In *JAXA Special Publication (in Japanese)*, pages 85–90, JAXA-SP-10-012, 2010.

[30] S. Obayashi and G. P. Guruswamy. Convergence Acceleration of an Aeroelastic Navier-Stokes Solver. *AIAA Journal*, 33(6):1134–1141, 1994.

[31] D. Sharov and K. Nakahashi. Reordering of Hybrid Unstructured Grids for Lower-Upper Symmetric Gauss-Seidel Computations. *AIAA Journal*, 36(3):484–486, 1998.

[32] A. K. Hellsten. New Advanced k-ω Turbulence Model for High-Lift Aerodynamics. *AIAA Journal*, 43(9):1857–1869, 2005.

[33] S. Wallin and A. V. Johansson. An Explicit Algebraic Reynolds Stress Model for Incompressible and Compressible Turbulent Flows. *Journal of Fluid Mechanics*, 403:89–132, 2000.

[34] J. C. R. Hunt, A. A. Wray, and P. Moin. Eddies, Streams, and Convergence Zones in Turbulent Flows. In *Proceedings of the Summer Program (Center for Turbulence Research, 1988)*, pages 193–208, 1988.